

Impact of horizontal resolution on the robustness of radiation emulators in a numerical weather prediction model

Hwan-Jin Song¹

¹National Institute of Meteorological Sciences, Korea Meteorological Administration

November 23, 2022

Abstract

Developing a radiation emulator based on machine learning in a weather forecasting model is valuable because it can significantly improve the computational speed of forecasting severe weather events. In order to fully replace the radiation parameterization in the weather forecasting model, the universal applicability of radiation emulator is essential, indicating a transition from the research to the operational level. This study addressed the universal issue of radiation emulators associated with horizontal resolutions from the climate simulation scale (100 km) to the cloud-resolving scale (0.25 km). All simulations were performed using an emulator trained at 5 km simulation. In real-case simulations (100–5 km), the forecast errors of radiative fluxes and precipitation were reduced at coarse resolutions. The ideal-case simulations (5–0.25 km) also showed a similar feature with increased errors in heating rates and fluxes at fine resolutions. However, all simulations maintained an appropriate accuracy range compared with observations in real-case simulations or the infrequent use of radiation parameterization in ideal-case simulations. These findings demonstrate the feasibility of a universal radiation emulator associated with different resolutions and models and emphasize the importance of future development directions toward the emulation of high-resolution modeling.

1 **Impact of horizontal resolution on the robustness of radiation emulators in**
2 **a numerical weather prediction model**

3
4
5
6
7
8
9 Hwan-Jin Song

10
11
12 National Institute of Meteorological Sciences, Korea Meteorological Administration, Jeju-do,
13 Republic of Korea

14
15
16
17 Submitted to Journal of Geophysical Research – Atmospheres (28 March 2022)

18
19
20 **Key Points**

- 21 - The universal applicability of the radiation emulator was examined at different resolutions
22 using two modeling frameworks.
23 - In both frameworks, the forecast errors at coarse resolutions were smaller than those at fine
24 resolutions.
25 - Because the stability of radiation emulator was universally maintained, and speed
26 improvement by the emulator can be highlighted.

27 _____
28 * *Corresponding author's address*

29 Hwan-Jin Song
30 National Institute of Meteorological Sciences,
31 63568, Seogwipo-si, Jeju-do, Republic of Korea
32 E-mail: hwanjinsong@gmail.com

33

34 **Abstract**

35 Developing a radiation emulator based on machine learning in a weather forecasting model is
36 valuable because it can significantly improve the computational speed of forecasting severe
37 weather events. In order to fully replace the radiation parameterization in the weather
38 forecasting model, the universal applicability of radiation emulator is essential, indicating a
39 transition from the research to the operational level. This study addressed the universal issue
40 of radiation emulators associated with horizontal resolutions from the climate simulation
41 scale (100 km) to the cloud-resolving scale (0.25 km). All simulations were performed using
42 an emulator trained at 5 km simulation. In real-case simulations (100–5 km), the forecast
43 errors of radiative fluxes and precipitation were reduced at coarse resolutions. The ideal-case
44 simulations (5–0.25 km) also showed a similar feature with increased errors in heating rates
45 and fluxes at fine resolutions. However, all simulations maintained an appropriate accuracy
46 range compared with observations in real-case simulations or the infrequent use of radiation
47 parameterization in ideal-case simulations. These findings demonstrate the feasibility of a
48 universal radiation emulator associated with different resolutions and models and emphasize
49 the importance of future development directions toward the emulation of high-resolution
50 modeling.

51 **Keywords:** WRF, RRTMG, radiation, resolution, neural network, emulator

52

53 **1. Introduction**

54 The atmospheric radiation process can be accurately expressed using line-by-line models
55 (Tjemkes et al., 2003; Clough et al., 2005; Kratz et al., 2005). However, it bears heavy
56 computation time, which limits its applicability. To overcome this challenge, machine-
57 learning emulators imitating radiative transfer processes have been actively developed.
58 Initially, it was confined to imitating the radiative transfer model (RTM) under specific
59 conditions (Chevallier et al., 1998; Liu et al., 2020; Ukkonen et al., 2020; Lagerquist et al.,
60 2021; Veerman et al., 2021; Meyer et al., 2022; Ukkonen, 2022). For RTM emulation studies,
61 advanced machine-learning techniques besides the common neural network (NN), such as the
62 random forest (Belochitski et al., 2011), the convolutional neural network (CNN; Liu et al.,
63 2020), the recurrent neural network (RNN; Ukkonen, 2022), and the U-net++ model
64 (Lagerquist et al., 2021), have been actively attempted. Emulation study applications have
65 completely replaced radiation parameterization in atmospheric forecasting models
66 (Krasnopolsky et al., 2005, 2008a, 2008b, 2010; 2012; Belochitski et al., 2011; Pal et al.,
67 2019; Roh and Song, 2020; Belochitski and Krasnopolsky, 2021; Song and Roh, 2021; Song
68 et al., 2021, 2022; Song and Kim, 2022). These emulator studies have shown sufficient speed
69 improvements of 10–100 times, compared with theoretical radiation schemes based on
70 discrete bands (Morcrette, 1991; Iacono et al., 2008; Baek, 2017; Hogan and Bozzo, 2018;
71 Pincus et al., 2019). All these emulators have been developed using the common NN with
72 single or multiple hidden layers because most radiation schemes and atmospheric forecasting
73 models are based on the Fortran software, and techniques besides the NN are difficult to
74 implement in the Fortran code. This case is different from the independent RTM case, which
75 is not linked with numerical prediction models such as the global climate model (GCM) and
76 numerical weather prediction (NWP) model.

77 The speed improvement by the RTM emulator was confined to the radiation process only.
78 In contrast, the radiation emulator in the NWP can further provide speedups for the entire
79 numerical prediction system, benefiting many applications (e.g., typhoon, flood, and heavy
80 snowfall) in which urgent weather forecasting is essential. In addition, because the radiation
81 emulator is linked to many dynamic and physical variables in the NWP or GCM, the
82 emulator can produce tremendous variables and outputs from radiative transfer processes at a
83 faster speed. Therefore, the radiation emulator in numerical prediction models is
84 incomparably valuable for broad applications compared to the RTM. Krasnopolsky et al.
85 (2005) first developed an NN emulator 50–80 times faster than the longwave (LW)
86 parameterization in the Community Atmospheric Model (CAM) with T42 resolution (~300
87 km). The emulation for shortwave (SW) parameterization, which was 20-fold faster, was
88 further included under the same CAM (Krasnopolsky et al., 2008a). Belochitski et al. (2011)
89 for different machine-learning methods and Krasnopolsky et al. (2008b) for compound
90 parameterization were conducted under the same CAM framework. NN emulators for both
91 LW and SW can improve the computational speed of radiative calculations by approximately
92 30 times and the total computation time by a maximum of 25% under the Climate Forecast
93 System (CFS) model with T126 resolution (~100 km) (Krasnopolsky et al., 2010). Pal et al.
94 (2019) developed an NN emulator with multiple hidden layers that can accelerate the
95 computational speed of the radiation process by a maximum of 10 times under a super-
96 parameterized energy exascale earth system model (SP-E3SM) with a 1° horizontal
97 resolution (~100 km). Krasnopolsky et al. (2012) further reported a speedup of approximately
98 37.5 times for the radiation process and a total reduction by a maximum of 18% under the
99 Global Forecast System (GFS) model with T574 resolution (~25 km). Recently, Belochitski
100 and Krasnopolsky (2021) demonstrated the universal performance of a radiation emulator
101 developed in the CFS model (Krasnopolsky et al., 2010) by applying it to the GFS model.

102 Although the current GFS model has a different horizontal resolution (~13 km) to 100 km of
103 the CFS, they kept the resolution as 100 km in the GFS experiment. In contrast to global
104 models, the radiation emulators for the Korean local model with a 5 km resolution called the
105 Korea Local Analysis and Prediction System (KLAPS; Shin et al., 2022) were developed,
106 showing a significant speedup of the radiation process by 60-fold and 87% reduction in total
107 computation time (Song and Roh, 2021; Song et al. 2021, 2022; Song and Kim, 2022).
108 Uniquely, Roh and Song (2020) developed a radiation emulator with speed improvements for
109 radiation process by 20–100 times and 82–86% reduction in total model time under a cloud-
110 resolving model (CRM) with a 0.25 km resolution. However, their result was limited to an
111 ideal case of a 6 h forecast in the daytime. Because previous studies on radiation emulators
112 were conducted in different modeling frameworks based on different horizontal resolutions
113 (from GCM to CRM), fully interpreting the meaning of the absolute errors found in the
114 literature is difficult. Therefore, the impact of the horizontal resolutions on the forecast
115 accuracy of the radiation emulator needs comprehensive investigation. To evaluate the
116 accuracy of emulator, various aspects need to be validated, such as a common comparison
117 between control simulations (Krasnopolsky et al., 2005, 2008a, 2008b, 2010, 2012;
118 Belochitski et al., 2011; Pal et al., 2019; Belochitski and Krasnopolsky, 2021) and
119 evaluations with the infrequent use of radiation parameterization and observations (Roh and
120 Son, 2020; Song and Roh, 2021; Song et al., 2021; Song et al., 2022; Song and Park, 2022).

121 Precipitation, the most important predictor in the weather forecasting model, is implicitly
122 determined by cumulus parameterization at coarse horizontal resolutions (e.g., above 100 km).
123 However, precipitation is explicitly calculated using cloud microphysics parameterization at
124 convection-permitting scales, typically at resolutions of several kilometers. Owing to the
125 spatial smoothing effect, precipitation forecasting at coarse resolution is generally more
126 accurate compared with that at fine resolution (Robert and Lean, 2008; Clark et al., 2016),

127 while high-resolution forecasting remains important. In contrast, the forecast accuracy at
128 coarse resolution for surface temperature is generally lower than that at fine resolution
129 (Pavlik et al., 2012; Kumar et al., 2016) because the smoothing effect at coarse resolution
130 hinders the realistic prediction of temperature variability. The contrast associated with
131 horizontal resolutions can lead to the conjecture that the radiation emulators developed in
132 climate models with 100–300 km resolutions (Krasnopolsky et al., 2005, 2008a, 2008b, 2010,
133 2012; Belochitski et al., 2011; Pal et al., 2019; Belochitski and Krasnopolsky, 2021) show
134 different behavior compared with those of the convection-permitting NWP model with 5 km
135 resolution (Song and Roh, 2021; Song et al., 2021, 2022; Song and Kim, 2022) or CRM with
136 0.25-km resolution (Roh and Song, 2020). Although it is not linked with numerical
137 forecasting models, emulation studies for the RTM used datasets based on horizontal
138 resolutions of 80 km (Liu et al., 2020; Ukkonen et al., 2020; Ukkonen, 2022), 30 km (Meyer
139 et al., 2022), 13 km (Lagerquist et al., 2021), and 1 km (Veerman et al., 2021). However,
140 these studies were developed using different numerical models and machine-learning
141 methods, and it is difficult to conclude which studies show more improved results.
142 Furthermore, the previous radiation emulators were evaluated under the same conditions as
143 the trained horizontal resolution. Because the horizontal resolution of datasets and targeting
144 models can be changed per institutional policy or users' interest from the trained version, the
145 universal robustness of the developed radiation emulator at different horizontal scales should
146 be satisfied for applying the emulator to various modeling systems with horizontal resolutions.

147 The universal applicability of radiation emulators, partially demonstrated by Belochitski
148 and Krasnopolsky (2021) and Song and Kim (2022), is associated with the changes in
149 numerical models (CFS to GFS) and microphysics parameterizations along with different
150 models (real-case to ideal-case simulations), respectively. However, the effect of the
151 horizontal resolution on the robustness of the radiation emulator remains unknown. Therefore,

152 this study aimed to investigate the universal performance of a radiation emulator with a 5 km
153 resolution developed by Song et al. (2022) when it was applied to different horizontal
154 resolutions for climate and cloud-resolving simulations (100 km to 0.25 km). As in Song and
155 Kim (2022), the trained results from three-dimensional real-case simulations were applied to
156 two-dimensional ideal-case simulations. We expect these quantitative analyses to provide
157 stability and accuracy in the operational NWP model, in association with the potential use of
158 a machine-learning radiation scheme. In addition, it can provide a comprehensive insight into
159 various radiation emulators developed at different resolutions, suggesting a future
160 development direction for radiation emulators.

161 **2. Data and Methods**

162 This study utilized the NN radiation scheme developed by Song et al. (2022) for the
163 KLAPS model over the Korean peninsula. The emulator imitated the RRTMG-K radiation
164 parameterization (Baek, 2017), an updated version of the Rapid Radiative Transfer Model for
165 GCMs (RRTMG; Iacono et al., 2008) with LW of 14 bands and 256 g points and SW of 16
166 bands and 224 g points, using NN training on 288 million input-output pairs throughout
167 2009–2019. Stochastic weight averaging (SWA; Izmailov et al., 2018) was applied during the
168 NN training. The LW/SW emulators for a certain month consisted of four categories: land,
169 ocean, clear, and cloudy. The input variables for the NN training were vertical profiles of
170 pressure, temperature, water vapor, ozone, and cloud fraction, in addition to skin temperature
171 and surface emissivity (LW), as well as insolation and surface albedo (SW). The output
172 variables used were heating rate profiles, upward fluxes at the top and bottom of the
173 atmosphere, and downward flux at the bottom. Hereafter, the LW/SW fluxes in this study
174 indicate the average of three fluxes at the top and bottom. The nonlinear relationship between
175 the inputs and outputs was approximated by the NN based on 90 neurons and single hidden
176 layer. As a result of NN training, weight and bias coefficients were obtained, which were

177 linked to the KLAPS model. The radiation emulator showed an approximately 60-fold
178 speedup compared to the RRTMG-K and 84–87% reduction of total computation time (Song
179 and Roh, 2021; Song et al., 2022).

180 The KLAPS model used in this study was primarily based on Advanced Research of the
181 Weather Research and Forecasting (WRF-ARW) model (Skamarock et al., 2019). The
182 physics suites other than radiation parameterization were the WRF double moment 7-Class
183 microphysics, Simplified Arakawa–Schubert cumulus modified by the Korea Institute of
184 Atmospheric Prediction Systems (KIAPS), Shin and Hong boundary layer, unified Noah land
185 surface model, and revised MM5 Monin–Obukhov surface layer (Skamarock et al., 2019).
186 The European Center for Medium-Range Weather Forecasts Reanalysis v5 (ERA5; Hersbach
187 et al., 2020) reanalysis data with 0.25° horizontal and 37 pressure-level resolutions were used
188 to simulate the WRF model in real cases. The real-case simulation was integrated by 7 d with
189 a 20 s time step over 5 km horizontal grids (234×282) based on the Lambert conformal conic
190 projection and 40 vertical levels. The real-case simulations were initialized from the 1st, 8th,
191 15th, 22nd days of each month in 2020, consisting of 48 weekly cases. For these cases, the LW
192 and SW fluxes at 3 h intervals were used to evaluate the forecast accuracy of the radiation
193 emulator by comparing the control simulation based on the original radiation
194 parameterization. The forecast accuracy using the emulator was also evaluated by comparing
195 it with surface observations in South Korea. The 2 m air temperature (T_{2m}) data were
196 measured from 713 stations, and precipitation data with 5 km resolution were derived by
197 merging rain gauges and ground-based radar measurements (Fig. 1). In addition, this study
198 considered a two-dimensional squall line experiment within the WRF model for an extreme
199 simulation (Skamarock et al., 2019). Although this is a case study, it corresponds to a highly-
200 unstable situation compared with the one-year average of the real-case simulations. For
201 example, the forecast errors of the LW/SW fluxes were 121% and 185% larger in the ideal-

202 case simulation than in the real case (Song and Kim, 2022). This ideal simulation was forced
203 by the default initial sounding in the WRF model and based on 201 horizontal and 40 vertical
204 levels. Furthermore, it was integrated for 24 h with a 3 s time step. The radiation emulator
205 developed in a real-case simulation (July and land) was applied to the ideal-case simulation to
206 test the robustness associated with the representation error (Song and Kim, 2022).

207 To analyze the effects of resolution on the universal performance of the radiation
208 emulator, simulations were performed at different spatial grids of 234×282 (5 km), 118×142
209 (10 km), 48×57 (25 km), 25×29 (50 km), 16×20 (75 km), and 13×15 (100 km), while
210 maintaining similar spatial coverage over the Korean peninsula. The trained results under 5
211 km resolution were applied to 10–100 km resolutions as a completely independent validation,
212 although the 5 km simulation was also evaluated for the independent period (2020) to the
213 training period (2009–2019). In previous studies (Song and Roh, 2021; Song et al., 2021,
214 2022; Song and Kim, 2022), the surrounding four points around the lateral boundary were
215 excluded from both training and testing because physically unrealistic data can appear around
216 the lateral boundary. However, because the 100 km simulation was performed in a small
217 domain, excluding the data around the lateral boundary was unfair between 5 km and 100 km
218 in terms of spatial coverage. Thus, this study included data around the lateral boundary by
219 modifying the width of the relaxation zone from four to one. For ideal-case simulation, 5, 3, 2,
220 1, 0.5, and 0.25 km resolutions were used while maintaining 201 horizontal grids.

221 **3. Results and Discussion**

222 *Previous studies under different resolutions*

223 There is a trade-off between accuracy and speedup in the emulator study; thus, the
224 accuracy of emulator should be compared under the same (or similar) computation conditions.
225 Because of this, using many neurons and hidden layers in the NN is a constraint leading to a
226 slowdown. Therefore, it is against the ultimate goal of the radiation emulator in CGMs and

227 NWPs. Even if a study showed better accuracy using an advanced machine-learning method,
228 an additional slowdown from the method should be carefully considered. In offline testing
229 (not linked to the NWP model) for a two-dimensional ideal simulation under 0.25 km
230 resolution, as an extreme case, the radiation emulator with a 57-fold speedup produced root
231 mean square errors (RMSEs) of 1.54 K day⁻¹ for LW heating rate and 1.13 K day⁻¹ for SW
232 heating rate (Roh and Song, 2020). For 288 million independent data in real-case simulations,
233 the NN radiation scheme developed under 5 km resolution with a 60-fold speedup (Song and
234 Roh, 2021) showed the RMSEs of 0.59 K day⁻¹ for LW heating rate, 0.22 K day⁻¹ for SW
235 heating rate, 4.41 W m⁻² for LW flux, and 20.72 W m⁻² for SW flux. These RMSEs were
236 further reduced by 0.46 K day⁻¹, 0.18 K day⁻¹, 3.59 W m⁻², and 19.13 W m⁻², respectively,
237 using SWA during the NN training (Song et al., 2022). In contrast, many previous studies
238 used the common NN (Krasnopolsky, 2014) based on a sequential training (Krasnopolsky et
239 al., 2005, 2008a, 2008b, 2010; Belochitski et al., 2011; Roh and Song, 2020; Belochitski and
240 Krasnopolsky, 2021; Song and Roh, 2021; Song et al., 2021). In CGM studies, the RMSEs
241 for LW and SW heating rates in the offline testing were 0.34 K day⁻¹ and 0.19 K day⁻¹ in 300
242 km resolution (CAM), 0.49 K day⁻¹ and 0.20 K day⁻¹ in 100 km resolution (CFS), and 0.52 K
243 day⁻¹ and 0.26 K day⁻¹ in 25 km resolution (GFS), respectively (Krasnopolsky et al., 2020,
244 2012). The radiation emulators for CFS and GFS were 30–40 times faster than that for
245 RRTMG, similar to RRTMG-K for targeting reported by Roh and Song (2020), Song and
246 Roh (2021), Song et al. (2021), Song et al. (2022), and Song and Kim (2022). Because the
247 CGM studies were performed in the same group using the same NN technique and input-
248 output structure, we suspect that the heating rate errors by the emulator reduced when the
249 horizontal resolution became coarse. The results of Krasnopolsky’s groups were obtained by
250 using 0.4 million data (both LW and SW) based on individual NN training for each GCM
251 model. Pal et al. (2019) used additional training datasets of 16.2 million. Furthermore, Song

252 and Roh (2021) and Song et al. (2022) used a large number of training sets (288 million data)
253 for a small area (i.e., Korea). Because the representation error can be reduced by using more
254 datasets covering natural variability, despite the 5 km resolution, the RMSEs of the LW and
255 SW heating rates in Song et al. (2022) were smaller than those in Krasnopolsky et al. (2010,
256 2012).

257 Numerical errors caused by a radiation emulator can be rapidly amplified during long-
258 term integration into CGMs or NWP (called online testing). For an ideal-case simulation
259 under 0.25 km resolution, the RMSEs of LW/SW fluxes were amplified by 135% and 72%
260 during 6 h forecasts (7200-time steps) compared with the offline testing results (Roh and
261 Song, 2020). For real-case simulation under 5 km resolution, the RMSEs for LW/SW fluxes
262 during 1 d forecasts (4320-time steps) increased by 84% and 136%, respectively (Song and
263 Roh, 2021). For 7 d forecasts (30240-time steps), the RMSEs for LW/SW fluxes were further
264 increased by 148% and 215%, respectively (Song et al., 2022). From these results, we expect
265 that the numerical errors of the radiation emulator can be amplified more in the case of
266 seasonal or inter-annual predictions based on the GCM. However, because the GCM
267 forecasts are evaluated at monthly or yearly scales in contrast to the hourly scale for the NWP
268 forecasts, error amplification by the long-term integration of the radiation emulator was
269 mostly hidden in previous GCM studies (Krasnopolsky et al., 2005, 2008a, 2008b, 2010,
270 2012; Belochitski et al., 2011; Pal et al., 2019; Belochitski and Krasnopolsky, 2021). For
271 example, although Belochitski and Krasnopolsky (2021) attempted a universal application of
272 the radiation emulator by applying the training results based on the 100-km CFS into the 100-
273 km GFS, they did not quantitatively evaluate the hourly scale (e.g., RMSE), except for global
274 mean bias showing systematic stability. Under 5 km resolution, the RMSEs of LW/SW
275 heating rates and fluxes for the radiation emulator of Song et al. (2022) can be magnified by
276 8.6%–41.3% if different microphysics schemes with the trained version are used (Song and

277 Kim, 2022). The one-year mean bias for LW and SW fluxes (-0.08 W m^{-2} and 0.57 W m^{-2}) in
278 Song and Kim (2022) was smaller than those (-0.26 W m^{-2} and 0.59 W m^{-2}) in Belochitski
279 and Krasnopolsky (2021), despite different resolutions (5 km vs. 100 km). From these
280 previous studies, we can conclude that the radiation emulator developed by Song et al. (2022)
281 is the most mature among the developed radiation emulators in terms of universal robustness..
282 This emulator also showed stable results when evaluated with surface temperature,
283 precipitation observations (Song et al., 2022), and the changes in 14 microphysics schemes
284 (Song and Kim, 2022).

285 *Real-case simulations*

286 The forecast accuracy of radiation emulator in the NWP model can be evaluated by
287 comparing the control simulations based on the original radiation parameterization or
288 observation data. To evaluate the accuracy of the LW/SW fluxes using a radiation emulator,
289 we utilized the framework used by Song et al. (2022) and Song and Kim (2022). This
290 framework considered 48 weekly cases (approximately one year) with a 3 h interval for
291 234×282 grids (5 km); thus, the statistics were obtained from 177,375,744 data points.
292 Because different domain sizes, such as 118×142 (10 km), 48×57 (25 km), 25×29 (50 km),
293 16×20 (75 km), and 13×15 (100 km), were considered for resolution experiments, the data
294 points used were also reduced in proportion to the domain size. The emulator results at
295 different resolutions were compared with each control simulation. T_{2m} and 3-hourly
296 accumulated precipitation simulated using the radiation emulator were compared with surface
297 observation data for the 48 weekly cases.

298 Figure 2 illustrates the spatial distributions of RMSEs for LW/SW fluxes when the
299 radiation emulator developed at 5 km resolution was applied to 10–100 km resolutions. The
300 WRF simulation results based on the Lambert conformal conic projection were interpolated
301 to the latitude-longitude projection with a regular grid interval to draw the plots. First, the

302 RMSEs of the LW flux showed a clear contrast between the land and ocean because the skin
303 temperature and surface emissivity, as inputs for the LW radiation process, were separated
304 between land and ocean. Furthermore, mountainous areas can represent a strong variability in
305 skin temperature toward colder temperatures than the surrounding low-latitude areas.
306 Because KLAPS models use a terrain-following vertical coordinate, and vertical profiles (e.g.,
307 pressure, temperature, and moisture) around the surface are affected by topographic altitudes.
308 For these reasons, the LW flux shows the largest error above 11 W m^{-2} in the Gaema Plateau
309 area in North Korea, having the highest topographic altitude (Fig. 2a). For the RMSEs of the
310 SW flux, the land–ocean contrast is unclear; it tends to slightly increase toward the southern
311 region (Fig. 2g). The more abundant cloud conditions and slightly larger insolation in the
312 southern region explain the error pattern of SW flux. In contrast, in the Chinese desert areas
313 located in the northwest, the lowest RMSEs for SW flux were found because of the low-cloud
314 condition. When the horizontal resolutions increased to 10, 25, 50, 75, and 100 km, the
315 RMSEs in both LW and SW dropped sharply. Because the radiation emulator used in this
316 study was trained at 5 km resolution, the results at different resolutions should produce
317 outputs with greater uncertainty in terms of representation error. However, the smoothing
318 effects for input-output variables contributed to producing more accurate results with a
319 universal application beyond the representation error at different resolutions. The lower
320 representation error could be due to using large training sets for the small Korean domain.
321 The number of training sets used by Song and Roh (2021) and Song et al. (2022) was 720
322 times larger than those used by Krasnopolsky et al. (2010, 2012) and Belochitski and
323 Krasnopolsky (2021). Because the GCM domain covers the entire globe, using more training
324 sets is essential to ensure universality and accuracy in the global region, similar to Song et al.
325 (2022). Therefore, we can conclude that the 5 km simulation results of Song and Roh (2021),
326 Song et al. (2021), Song et al. (2022), and Song and Kim (2022) were developed under more

327 difficult condition to secure the universality of radiation emulators compared with 25 km
328 resolution (Krasnopolsky et al., 2012) and resolutions larger than 100 km (Krasnopolsky et
329 al., 2005, 2008a, 2008b, 2010; Belochitski et al., 2011; Pal et al., 2019; Belochitski and
330 Krasnopolsky, 2021). Similarly, we can expect that the development of a radiation emulator
331 at resolutions less than 5 km, such as the 0.25 km resolution in Roh and Song (2020), would
332 be more difficult. Because of the limitation of computational resources, although this study
333 did not consider real-case simulations at resolutions less than 5 km, this issue will be dealt
334 with in the ideal-case simulation framework.

335 Figure 3 shows the temporal variations in RMSEs for LW/SW fluxes, T_{2m} , and 3-hourly
336 accumulated precipitation during the 7-day forecasts averaged from the total 48 weekly cases
337 and entire domain. The RMSEs of the LW flux increase steadily with forecast time while
338 showing diurnal variation between night and day (Fig. 3a). Because the variability in surface
339 temperature is larger during the daytime, the RMSEs of the LW flux also show an amplified
340 error during the day. The RMSEs of the SW flux are characterized by a strong diurnal
341 variation associated with the evident diurnal cycle of insolation while showing a gradual
342 increase in error with forecast time (Fig. 3b). In both LW and SW fluxes, the RMSEs at
343 coarse resolutions were lower than those at fine resolutions. For resolutions larger than 50 km,
344 the RMSE patterns in the LW flux tended to be saturated (Fig. 3a); similar trends are found in
345 the spatial distribution (Figs. 2d–f). The total RMSEs for the three LW and SW fluxes are
346 listed in Table 1. The RMSEs of LW and SW fluxes for 5, 10, 25, 50, 75, and 100 km were
347 9.59, 9.16, 8.16, 7.79, 7.78, and 7.99 $W m^{-2}$ and 63.17, 60.34, 52.78, 49.03, 46.89, and 47.40
348 $W m^{-2}$, respectively. Accordingly, the 5-km results were more uncertain by 20% (LW) and 33%
349 (SW) compared with the 100-km results. If the results were re-trained at each resolution, not
350 aiming at the universal application of the 5-km radiation emulator, the difference between the
351 5-km and 100-km results would have been more. These results show that the 5-km

352 simulations in Song and Roh (2021), Song et al. (2021), Song et al. (2022), and Song and
353 Kim (2022) were harsher environments than resolutions larger than 100 km (Krasnopolsky et
354 al., 2005, 2008a, 2008b, 2010; Belochitski et al., 2011; Pal et al., 2019; Belochitski and
355 Krasnopolsky, 2021). The evaluation results compared with the observation data revealed the
356 contrast between T_{2m} and precipitation (Figs. 3c–d). The RMSEs of T_{2m} increased with
357 increasing resolution (2.2619 K to 2.9405 K in Table 1), whereas an opposite trend was found
358 for the 3-hourly precipitation (1.5515 mm to 1.1479 mm in Table 1). When the horizontal
359 resolution is coarse, the spatial variability of the surface temperature in the model simulation
360 can be reduced from actual observations. Thus, overly coarse resolutions can degrade the
361 forecast accuracy of surface temperature. Pavlik et al. (2012) and Kumar et al. (2016)
362 reported similar results, showing lower accuracy at coarse resolution for surface temperature.
363 Because precipitation forecast is highly uncertain, the smoothing effect at a coarse resolution
364 can be more important in determining the forecast error of precipitation. The forecast skill of
365 precipitation in numerical models was rather improved at coarse horizontal scales (Robert
366 and Lean, 2008; Clark et al., 2016). This illusion effect at coarse resolution does not indicate
367 that high-resolution modeling is unnecessary.

368 The role of cumulus parameterization in determining precipitation and surface
369 temperature is more important at coarse resolutions than at fine resolutions. Therefore, we
370 need to examine the behavior of radiation emulator results with a turned-off cumulus scheme.
371 To turn off the cumulus scheme, the RMSEs for LW/SW fluxes and T_{2m} in Table 1 were
372 changed by a maximum 0.9% (at 100 km resolution), while the general trends were
373 unchanged. The RMSEs of the 3-hourly precipitation forecasts at 100 km resolution were
374 changed the most by 6.7%, resulting in 0.2472 mm. Nevertheless, these results do not affect
375 the conclusion of this study regarding the universal application of a radiation emulator.
376 Furthermore, readers may suspect that the observational evaluations in Table 1 are a

377 characteristic of the radiation emulator. However, the control simulations based on the
378 original radiation parametrization showed similar RMSEs for T_{2m} (2.2619 K to 2.9895 K) and
379 3-hourly precipitation (1.5641 mm to 1.1433 mm). Therefore, we can conclude that the
380 radiation emulator developed at 5 km resolution can be universally applied for horizontal
381 resolutions larger than 5 km while maintaining the accuracy and stability. However, the
382 opposite situation (coarse to fine resolutions) cannot be guaranteed because the potential error
383 from the radiation emulator can lead to unstable results in numerical models (Krasnopolsky et
384 al., 2008b; Song et al., 2021; Belochitski and Krasnopolsky, 2021; Song and Kim, 2022).
385 This drawback led to the next analysis based on ideal-case simulations.

386 *Ideal-case simulations*

387 Considering a tremendous computation resource for long-term simulations at fine
388 resolutions less than 5 km, the universal application of a radiation emulator at 5 to 0.25 km
389 resolutions was evaluated in a two-dimensional idealized squall line simulation as an extreme
390 precipitating case. Similar ideal simulations were conducted by Roh and Song (2020), Song
391 et al. (2022), and Song and Kim (2021). Song and Kim (2021) examined the universal
392 application of a radiation emulator with changes in 14 additional microphysics schemes at 5
393 km resolution. As a follow-up, this study examined the effects of horizontal resolution on a
394 universal radiation emulator. The radiation emulator used in this study was obtained from
395 real-case simulations (July and land). This study considered a 24-hour integral period with a
396 3-s time step; hence, the emulator was applied four times more than Roh and Song (2020) for
397 a 6-hour forecast and 6.66 times more than Song et al. (2022) and Song and Kim (2022)
398 using a 20 s time step. A 3 s time step was essential for the control simulation at 0.25 km (the
399 use of larger time step led to a blow up of the control simulation). Comparing the
400 representation error of the real-case simulation to the ideal case, the RMSEs of the radiation
401 emulator in Song and Kim (2022) were larger by 23%–48% than the infrequent use of

402 radiation parameterization by 60 times in Song et al. (2022). Because an ideal simulation is
403 an extreme case, the error caused by the emulator can be rapidly amplified. Accordingly, the
404 RMSEs of the radiation emulator in Table 2 appear moderately large. These RMSEs were
405 calculated for 201 horizontal grids and 1440 temporal data points at 10 m intervals. The
406 heating rate and flux in this study represent the average of 39 vertical layers and three flux
407 components (at top and bottom), respectively. To minimize the error associated with
408 universal representation, Song and Kim (2022) attempted compound parameterization (CP),
409 returning the original parameterization when the predicted heating-rate errors exceeded a
410 predefined threshold. They used thresholds of 1.0341 and 0.4820 K day⁻¹ for LW and SW
411 heating rates, respectively, to target an approximately 3-fold slowdown to the emulator with
412 60-fold speedup. When the same concept was applied in this study, the emulator + CP results
413 were 3.23–4.21 times slower than the emulator only. This result implies that the emulator +
414 CP is still 14–19 times faster than the original radiation parameterization. By adding CP, the
415 total RMSEs at 5 km resolution was reduced by 27.3%, 26.7%, 22.3%, and 16.8% for the LW
416 heating rate, SW heating rate, LW flux, and SW flux, respectively. The resulting RMSEs of
417 heating rates (2.61 K day⁻¹ and 1.21 K day⁻¹) are comparable to 2.57 K day⁻¹ and 1.20 K day⁻¹
418 based on the infrequent use of radiation parameterization by 30 times (Song et al., 2022).
419 These results indicate that using a radiation emulator along with CP can maintain stable
420 accuracy while overcoming the representation error induced by the difference between real
421 and ideal cases, as well as different horizontal resolutions. The successful results of this study
422 associated with universal robustness are novel and worthy of recognition.

423 Figure 4 displays the temporal and spatial variations of outgoing LW radiation (OLR) and
424 upward LW flux at the top of the atmosphere for 5, 3, 2, 1, 0.5, and 0.25 km resolutions. Each
425 simulation had the same number of horizontal grids but different coverage areas from 1000
426 km to 50 km. The difference in area coverage induced different evolutionary patterns among

427 the control simulations. A low OLR indicates vigorous deep convection, whereas a high OLR
428 represents a clear condition. While the 5-km control simulation is characterized by widely
429 spread clear areas (expressed by high OLR values) before hour 12 (Fig. 4a), the clear sky
430 portion is rapidly reduced when the horizontal resolution decreases from 5 to 0.25 km. At
431 0.25 km, there are small clear areas before hour 1. Because cloud simulation is uncertain in
432 the radiation parameterization, the 0.25-km simulation corresponds to a more highly
433 nonlinear situation than the 5-km simulation. The sharp effect at a fine resolution (in contrast
434 to smoothing effect at a coarse resolution) provides a more uncertain situation at 0.25-km
435 resolution. For these reasons, the occurrence frequencies of lower OLRs, regarded as deep
436 convective clouds, are higher at fine resolutions in both real and ideal cases (Fig. 5). In
437 contrast to the long-term (one year) results for the real case showing a stable smoothing effect
438 with resolution (Fig. 5a), the ideal simulations based on one case show great variability in
439 probability density functions (Fig. 5b). Because of the sharp effect and high cloud conditions
440 at fine resolutions, the occurrence frequencies of OLRs less than 180 W m^{-2} were higher at
441 fine resolutions, whereas those around 270 W m^{-2} , regarded as a clear condition, were
442 relatively reduced at fine resolutions. Characteristically, the 0.25-km simulation showed a
443 rare occurrence with OLRs less than 180 W m^{-2} . In contrast, it showed frequent occurrences
444 with OLRs in the range of $180\text{--}220 \text{ W m}^{-2}$, compared with other fine resolutions (2 km, 1 km,
445 and 0.5 km). As shown in blue colors in Fig. 4f, the 0.25-km simulation produced medium
446 OLRs of $180\text{--}220 \text{ W m}^{-2}$ after 12 h. Accordingly, this is the result of nonlinear characteristics
447 in the cloud-resolving simulation.

448 With these control simulation characteristics, the radiation emulators (along with CP)
449 successfully reproduce similar features to the control simulations until 24 h (Figs. 4g–i). The
450 ideal simulation is sensitive to small initial perturbations and rapidly changed during
451 integration; therefore, obtaining accurate plots for Figs. 4g–i is difficult. The clear area in the

452 initial stage at coarse resolutions and the subsequent widely spread clouds are realistically
453 expressed in the emulator results, despite the results being trained from real-case simulations.
454 The difference between control and emulator results tended to be larger at fine resolutions.
455 For example, OLRs higher than 200 W m^{-2} after 20 h in the control simulation at 0.25 km are
456 not found in the 0.25-km emulator result. Figure 6 illustrates the vertical RMSEs of the
457 heating rates and temporal RMSEs of the fluxes. The RMSEs were calculated for the total
458 temporal-horizontal grids and horizontal grids, respectively. The 1-km and 0.5-km
459 simulations show a larger error in the heating rates at middle levels (Figs. 6a–b). The 0.5-km
460 simulation is also characterized by a large error in the LW heating rate around the surface
461 (Fig. 6a). For the LW flux, no characteristic features were observed at a specific resolution
462 (Fig. 6c). The RMSE of the SW flux is the largest in the 0.25-km simulation, especially
463 around 15–16 h. In contrast, the RMSEs for 1-km and 0.5-km simulations are
464 characteristically lower than those for coarse resolutions (Fig. 6d). The total RMSE statistics
465 are listed in Table 2. Because the ideal simulation is a highly nonlinear process, a consistent
466 tendency with resolutions, such as in the real case, is not found. In general, increasing errors
467 at fine resolutions using an emulator are evident. Compared with the 5-km simulation, for the
468 0.25–3 km resolutions, the errors of the LW heating rate, SW heating rate, LW flux, and SW
469 flux increased by 19%–128%, 41%–104%, 11%–123%, and 17%–57%, respectively,. These
470 errors increase with horizontal resolutions and are larger than those induced by changes in
471 microphysics parameterization at 5-km resolution in Song and Kim (2022). By using CP, the
472 increased RMSE in the LW and SW heating rates are further reduced by 13%–72% and 9%–
473 45%, respectively, compared with the 5-km simulation. For LW and SW fluxes, the RMSEs
474 were improved by a maximum of 6% and 37%, respectively, in coarse resolutions. These
475 features are closely related to the CP because using CP contributed more to the improvements
476 in LW/SW fluxes (25%–35% and 27%–52%) than LW/SW heating rates (22%–67% and

477 17%–64%), especially for 1 km and 0.5 km resolutions. Although the RMSEs are higher at
478 fine resolutions than at coarse resolutions, this study is not the blow-up issue of the entire
479 model, such as the unphysical OLR in Belochitski and Krasnopolsky (2021). Therefore, we
480 can conclude that the radiation emulator developed at 5 km resolution can be universally
481 applied for cloud-resolving resolutions less than 5 km while maintaining accuracy at the
482 expense of computational speed by using CP (i.e., 60-fold to 14–19-fold speedup).

483 **4. Summary and Conclusions**

484 In this study, we considered different horizontal resolutions under two simulation
485 frameworks: KLAPS over the Korean peninsula (real case) and two-dimensional squall line
486 simulation (ideal case) to examine the impact of horizontal resolution on the universal
487 applicability of the radiation emulator in NWP models. The real-case simulation was
488 performed for approximately one year with a 7 d forecast time, whereas the ideal-case
489 simulation was an extreme squall line case with a 1 d forecast time. The horizontal
490 resolutions were 5, 10, 25, 50, 75, and 100 km (convection-permitting scale to climate
491 simulation scale) for the real-case simulation and 5, 3, 2, 1, 0.5, and 0.25 km (convection-
492 permitting scale to cloud-resolving scale) for the ideal-case simulations. All emulator
493 simulations were based on the NN radiation scheme developed under the real-case at 5-km
494 simulations by Song et al. (2022). This emulator was 60-fold faster than the RRTMG-K
495 radiation parameterization. Here, all simulations were tested in an independent period using
496 training sets (2009–2019). The real-case simulation focused only on the impact of horizontal
497 resolutions on the universal applicability of the 5-km radiation emulator. In contrast, the
498 ideal-case simulation further considered the universal robustness arising from the difference
499 between the real and ideal cases. Despite the different horizontal resolutions with the trained
500 5-km resolution, the forecast error of LW/SW fluxes was significantly reduced from fine to
501 coarse resolutions (9.59 to 7.79 W m⁻² and 63.17 to 46.89 W m⁻²). In addition, the RMSEs of

502 T_{2m} and precipitation, compared with the observations, increased and decreased from fine to
503 coarse resolutions (2.2619 K to 2.9405 K and 1.5515 mm to 1.1479 mm), respectively.
504 Because control simulations also showed the same error characteristic for T_{2m} , these results
505 suggested that the radiation emulator developed at a 5 km resolution is universally applied for
506 horizontal resolutions larger than 5 km while maintaining accuracy and stability. For the
507 ideal-case simulation, the temporal and spatial evolutions of the OLRs were examined for
508 different horizontal resolutions (5, 3, 2, 1, 0.5, and 0.25 km). Each control simulation showed
509 a large difference in the temporal and spatial cloud patterns owing to the smoothing effect at
510 coarse resolutions and different cloud conditions. Using radiation emulator successfully
511 reproduces features similar to those of the control simulations. For 0.25–3 km resolutions, the
512 forecast errors of the LW heating rate, SW heating rate, LW flux, and SW flux increased by
513 19–128%, 41–104%, 11–123%, and 17–57%, respectively, compared with the 5-km
514 simulation. To minimize these errors, the compound parameterization 3.23–4.21 times slower
515 than the emulator was further used (i.e., 14–19 times faster than the original radiation
516 parameterization). By adding CP, the total RMSEs at 5 km resolution was reduced by 27.3%,
517 26.7%, 22.3%, and 16.8% for the LW heating rate, SW heating rate, LW flux, and SW flux,
518 respectively. The resulting RMSEs of LW heating rate, SW heating rate, LW flux, and SW
519 flux at 5–0.25 km resolutions were 2.61 to 4.49 $W m^{-2}$, 1.21 to 1.75 $W m^{-2}$, 15.60 to 17.65 W
520 m^{-2} , and 101.52 to 174.04 $W m^{-2}$, respectively. Here, the resulting RMSEs of heating rates at
521 5 km resolution (2.61 and 1.21 $K day^{-1}$) were comparable to 2.57 and 1.20 $K day^{-1}$ based on
522 the infrequent use of original radiation parameterization by 30 times (Song et al., 2022).

523 This study provides a comprehensive insight into radiation emulator studies using
524 numerical prediction models at different resolutions. From this study, it was found that
525 coarse-resolution modeling was easier than fine-resolution simulation to ensure the accuracy
526 and stability of the radiation emulator. Therefore, previous emulator studies at convection-

527 permitting and cloud-resolving scales were regarded as more valuable than low-resolution
528 studies based on climate models. In addition, these results provide important information on
529 the universal applicability of radiation emulators associated with using different horizontal
530 resolutions and modeling platforms. Although the universal robustness of the radiation
531 emulator has already been examined for changes in numerical models and microphysics
532 parameterization (Belochitski and Krasnopolsky, 2021; Song and Kim, 2022), no
533 experiments at a different resolution from the trained resolution have been conducted. The
534 efforts in this study are particularly variable as this study is the first to show the universal
535 applicability of radiation emulators at different resolutions. Therefore, the complete
536 replacement of radiation parameterization by a machine-learning emulator with a significant
537 speedup is nearing. This study can also accelerate the computational speed of regional
538 climate simulations or high-resolution modeling in terms of a faster radiation scheme. The
539 findings in this study also suggest an evident direction for developing the universal radiation
540 emulator in the future that it should be developed at a resolution as high as possible. The
541 emulator trained at low resolution has a great uncertainty when it is applied to high-resolution
542 model, because the occurrence frequency of extreme far corner events is underestimated at
543 the low-resolution modeling. In terms of universal application, one drawback of this study
544 confined to the Korean peninsula can be improved by expanding the training sets for global
545 regions.

546 **Acknowledgements**

547 This work was funded by the KMA Research and Development Program “Developing of AI
548 technology for weather forecasting” under Grant (KMA2021-00120).

549 **Data Availability Statement**

550 The radiation emulators used in this study and associated WRF modeling systems are
551 available in <https://doi.org/10.5281/zenodo.5638436> and
552 <https://doi.org/10.5281/zenodo.6033618>, respectively.

553 References

- 554 Baek, S. (2017). A revised radiation package of G-packed McICA and two-stream
555 approximation: Performance evaluation in a global weather forecasting model. *Journal*
556 *of Advances in Modeling Earth Systems*, 9, 1628–1640.
557 <https://doi.org/10.1002/2017MS000994>.
- 558 Belochitski, A., Binev, P., DeVore, R., Fox-Rabinovitz, M., Krasnopolsky, V., & Lamby, P.
559 (2011). Tree approximation of the long wave radiation parameterization in the NCAR
560 CAM global climate model. *Journal of Computational and Applied Mathematics*, 236,
561 447–460. <https://doi.org/10.1016/j.cam.2011.07.013>.
- 562 Belochitski, A., & Krasnopolsky, V. (2021). Robustness of neural network emulations of
563 radiative transfer parameterizations in a state-of-the-art General Circulation Model.
564 *Geoscientific Model Development*, 14, 7425–7437. [https://doi.org/10.5194/gmd-2021-](https://doi.org/10.5194/gmd-2021-114)
565 114.
- 566 Chevallier, F., Chéruy, F., Scott, N. A., & Chédin, A. (1998). A neural network approach for
567 a fast and accurate computation of a longwave radiative budget. *Journal of Applied*
568 *Meteorology*, 37, 1385–1397. [https://doi.org/10.1175/1520-0450\(1998\)037](https://doi.org/10.1175/1520-0450(1998)037).
- 569 Clark, P., Roberts, N., Lean, H., Ballard, S. P., & Charlton-Perez, C. (2016). Convection-
570 permitting models: a step-change in rainfall forecasting. *Meteorological Applications*,
571 23, 165–181. <https://doi.org/10.1002/met.1538>.
- 572 Clough, S. A., Shephard, M. W., Mlawer, E. J., Delamere, J. S., Iacono, M. J., Cady-Pereira,
573 K., Boukabara, S., & Brown, P. D. (2005). Atmospheric radiative transfer modeling: a
574 summary of the AER codes. *Journal of Quantitative Spectroscopy and Radiative*
575 *Transfer*, 91, 233–244. <https://doi.org/10.1016/j.jqsrt.2004.05.058>.
- 576 Hersbach, H., Bell, B., Berrisford, P., Hirahara, S., Horányi, A., Muñoz-Sabater, J., Nicolas,
577 J., Peubey, C., Radu, R., Schepers, D., Simmons, A., Soci, C., Abdalla, S., Abellan, X.,
578 Balsamo, G., Bechtold, P., Biavati, G., Bidlot, J., Bonavita, M., Chiara, G., Dahlgren, P.,
579 Dee, D., Diamantakis, M., Dragani, R., Flemming, J., Forbes, R., Fuentes, M., Geer, A.,
580 Haimberger, L., Healy, S., Hogan, R. J., Hólm, E., Janisková, M., Keeley, S., Laloyaux,
581 P., Lopez, P., Lupu, C., Radnoti, G., Rosnay, P., Rozum, I., Vamborg, F., Villaume, S.,
582 Thépaut, J.-N. (2020). The ERA5 global reanalysis. *Quarterly Journal of the Royal*
583 *Meteorological Society*, 146, 1999–2049. <https://doi.org/10.1002/qj.3803>.
- 584 Hogan, R. J., & Bozzo, A. (2018). A flexible and efficient radiation scheme for the ECMWF
585 model. *Journal of Advances in Modeling Earth Systems*, 10(8), 1990–2008.
586 <https://doi.org/10.1029/2018ms001364>.
- 587 Iacono, M. J., Delamere, J. S., Mlawer, E. J., Shephard, M. W., Clough, S. A., & Collins, W.
588 D. (2008). Radiative forcing by long-lived greenhouse gases: Calculations with the AER

- 589 radiative transfer models. *Journal of Geophysical Research*, 113, D13103.
590 <https://doi.org/10.1029/2008JD009944>.
- 591 Izmailov, P. Podoprikin, D., Garipov, T., Vetrov, D., and Wilson, A. G. (2018). Averaging
592 weights leads to wider optima and better generalization. *Conference on Uncertainty in*
593 *Artificial Intelligence (UAI) 2018*. <https://arxiv.org/abs/1803.05407>.
- 594 Krasnopolsky, V. M., Fox-Rabinovitz, M. S., & Chalikov, D. V. (2005). New approach to
595 calculation of atmospheric model physics: Accurate and fast neural network emulation
596 of longwave radiation in a climate model. *Monthly Weather Review*, 133, 1370–1383.
597 <https://doi.org/10.1175/MWR2923.1>.
- 598 Krasnopolsky, V. M., Fox-Rabinovitz, M. S., & Belochitski, A. A. (2008a). Decadal climate
599 simulations using accurate and fast neural network emulation of full, longwave and
600 shortwave, radiation. *Monthly Weather Review*, 136, 3683–3695.
601 <https://doi.org/10.1175/2008mwr2385.1>.
- 602 Krasnopolsky, V. M., Fox-Rabinovitz, M. S., Tolman, H. L., & Belochitski, A. A. (2008b).
603 Neural network approach for robust and fast calculation of physical processes in
604 numerical environmental models: Compound parameterization with a quality control of
605 larger errors. *Neural Networks*, 21, 535–543.
606 <https://doi.org/10.1016/j.neunet.2007.12.019>.
- 607 Krasnopolsky, V. M., Fox-Rabinovitz, M. S., Hou, Y. T., Lord, S. J., & Belochitski, A. A.
608 (2010). Accurate and fast neural network emulations of model radiation for the NCEP
609 coupled Climate Forecast System: Climate simulations and seasonal predictions.
610 *Monthly Weather Review*, 138, 1822–1842. <https://doi.org/10.1175/2009MWR3149.1>.
- 611 Krasnopolsky, V. M., Belochitski, A. A., Hou, Y. T., Lord, S. J., & Yang, F. (2012).
612 Accurate and fast neural network emulations of long and short wave radiation for the
613 NCEP Global Forecast System model. NCEP/NWS, NOAA, office note 471.
614 <https://www.emc.ncep.noaa.gov/officenotes/newernotes/on471.pdf>.
- 615 Krasnopolsky, V. M. (2014). NCEP neural network training and validation system: Brief
616 description of NN background and training software. Environment Modeling Center,
617 NCEP/NWS, NOAA. <https://doi.org/10.7289/v5qr4v2z>.
- 618 Kratz, D. P., Mlynczak, M. G., Mertens, C. J., Brindley, H., Gordley, L. L., Martin-Torres, J.,
619 Ferenc, M. M., & Turner, D. D. (2005). An inter-comparison of far-infrared line-by-line
620 radiative transfer models. *Journal of Quantitative Spectroscopy and Radiative Transfer*,
621 90(3-4), 323–341. <https://doi.org/10.1016/j.jqsrt.2004.04.006>.
- 622 Kumar, P., Ojha, S. P., Singh, R., Kishtawal, C. M., & Pal, P. K. (2016). Performance of
623 weather research and forecasting model with variable horizontal resolution. *Theoretical*
624 *and Applied Climatology*, 126, 705–713. <https://doi.org/10.1007/s00704-015-1607-7>.
- 625 Lagerquist, R., Turner, D., Ebert-Uphoff, I., Stewart, J., & Hagerty, V. (2021). Using deep
626 learning to emulate and accelerate a radiative transfer model. *Journal of Atmospheric*
627 *and Oceanic Technology*, 38, 1673–1696. <https://doi.org/10.1175/JTECH-D-21-0007.1>.

- 628 Liu, Y., Caballero, R., & Monteiro, J. M. (2020). RadNet 1.0: exploring deep learning
629 architectures for longwave radiative transfer. *Geoscientific Model Development*, 13,
630 4399–4412. <https://doi.org/10.5194/gmd-13-4399-2020>.
- 631 Meyer, D., Hogan, R. J, Dueben, P. D, & Mason, S. L. (2022). Machine learning emulation
632 of 3D cloud radiative effects. *Journal of Advances in Modeling Earth Systems*,
633 e2021MS002550, <https://doi.org/10.1029/2021MS002550>.
- 634 Morcrette, J.-J. (1991). Radiation and cloud radiative properties in the European Centre for
635 Medium Range Weather Forecasts forecasting system. *Journal of Geophysical Research*,
636 96(D5), 9121. <https://doi.org/10.1029/89jd01597>.
- 637 Pal, A., Mahajan, S., & Norman, M. R. (2019), Using deep neural networks as cost-effective
638 surrogate models for Super-Parameterized E3SM radiative transfer. *Geophysical*
639 *Research Letters*, 46, 6069–6079. <https://doi.org/10.1029/2018GL081646>.
- 640 Pincus, R., Mlawer, E. J., & Delamere, J. S. (2019). Balancing accuracy, efficiency, and
641 flexibility in radiation calculations for dynamical models. *Journal of Advances in*
642 *Modeling Earth Systems*, 11, 3087–3089. <https://doi.org/10.1029/2019MS001621>.
- 643 Pavlik, D., Söhl, D., Pluntke, T., Mykhnovych, A., & Bernhofer, C. (2012). Dynamic
644 downscaling of global climate projections for eastern Europe with a horizontal
645 resolution of 7 km. *Environmental Earth Sciences*, 65, 1475–1482.
646 <https://doi.org/10.1007/s12665-011-1081-1>.
- 647 Roberts, N. M., & Lean, H. W. (2008). Scale-selective verification of rainfall accumulations
648 from high-resolution forecasts of convective events. *Monthly Weather Review*, 136, 78–
649 97. <https://doi.org/10.1175/2007MWR2123.1>.
- 650 Roh, S., & Song, H.-J. (2020). Evaluation of neural network emulations for radiation
651 parameterization in cloud resolving model. *Geophysical Research Letters*, 47,
652 e2020GL089444. <https://doi.org/10.1029/2020GL089444>.
- 653 Shin, H.-C., Ha, J.-H., Ahn, K. D., Lee, E. H., Kim, C. H., Lee, Y. H., & Clayton, A. (2022).
654 An overview of KMA's operational NWP data assimilation system. In: Park, S. K. & Xu,
655 L. (eds) *Data Assimilation for Atmospheric, Oceanic and Hydrologic Applications (Vol.*
656 *IV)*. Springer, Cham. https://doi.org/10.1007/978-3-030-77722-7_26.
- 657 Skamarock, W. C., Klemp, J. B., Dudhia, J., Gill, D. O., Liu, Z., Berner, J., Wang, W.,
658 Powers, J. G., Duda, M. G., Barker, D. M., & Huang, X.-Y. (2019). A description of the
659 Advanced Research WRF model version 4. *NCAR Technical Notes*.
660 <https://doi.org/10.5065/1DFH-6P97>.
- 661 Song, H.-J., & Roh, S. (2021). Improved weather forecasting using neural network emulation
662 for radiation parameterization. *Journal of Advances in Modeling Earth Systems*, 13,
663 e2021MS002609. <https://doi.org/10.1029/2021MS002609>.
- 664 Song, H.-J., Roh, S., & Park, H. (2021). Compound parameterization to improve the accuracy
665 of radiation emulator in a numerical weather prediction model. *Geophysical Research*
666 *Letters*, 48, e2021GL095043. <https://doi.org/10.1029/2021GL095043>.

- 667 Song, H.-J., Roh, S., Lee, J., Nam, G., Yun, E., Yoon, J., & Kim, P. S., (2022). Benefits of
668 stochastic weight averaging in developing neural network radiation scheme for
669 numerical weather prediction. *Journal of Advances in Modeling Earth Systems*,
670 <https://doi.org/10.1002/essoar.10508964.1>. (in minor revision)
- 671 Song, H.-J., & Kim, P. S. (2022). Effects of cloud microphysics on the universal performance
672 of neural network radiation scheme. *Geophysical Research Letters*,
673 <https://doi.org/10.1002/essoar.10510634.1>. (in revision)
- 674 Tjemkes, S. ., Patterson, T., Rizzi, R., Shephard, M., Clough, S., Matricardi, M., Haigh, J. D.,
675 Höpfner, M., Payan, S., Trotsenko, A., Scott, N., Rayer, P., Taylor, J. P., Clerbaux, C.,
676 Strowl L. L., DeSouza-Machado, S., Tobin, D., & Knuteson, R. (2003). The ISSWG
677 line-by-line inter-comparison experiment. *Journal of Quantitative Spectroscopy and*
678 *Radiative Transfer*, 77(4), 433–453. [https://doi.org/10.1016/s0022-4073\(02\)00174-7](https://doi.org/10.1016/s0022-4073(02)00174-7).
- 679 Ukkonen, P., Pincus, R., Hogan, R. J., Nielsen, K. P., & Kaas, E. (2020). Accelerating
680 radiation computations for dynamical models with targeted machine learning and code
681 optimization. *Journal of Advances in Modeling Earth Systems*, 12, e2020MS002226.
682 <https://doi.org/10.1029/2020MS002226>.
- 683 Ukkonen, P. (2022). Exploring pathways to more accurate machine learning emulation of
684 atmospheric radiative transfer. *Journal of Advances in Modeling Earth Systems*,
685 e2021MS002875, <https://doi.org/10.1029/2021MS002875>.
- 686 Veerman M. A., Pincus, R., Stoffer, R., van Leeuwen, C. M., Podareanu, D., & van
687 Heerwaarden, C. C. (2021). Predicting atmospheric optical properties for radiative
688 transfer computations using neural networks. *Philosophical Transactions of the Royal*
689 *Society A*, 379, 20200095. <https://doi.org/10.1098/rsta.2020.0095>.
- 690
- 691

692 **Table 1.** Total root mean square error (RMSE) statistics for real-case simulations. The LW
 693 and SW fluxes [$W m^{-2}$], along with three upward (\uparrow) and downward (\downarrow) fluxes at the top and
 694 bottom, were compared with the control model simulations, whereas 2-m temperature (T_{2m})
 695 [K] and 3-hourly precipitation [mm] were compared with surface observations.

	5 km	10 km	25 km	50 km	75 km	100 km
LW flux	9.5888	9.1575	8.1587	7.7853	7.7776	7.9902
- top \uparrow	11.2884	10.6651	9.2559	8.8752	9.2227	9.8026
- bottom \uparrow	3.8179	3.7173	3.4111	3.3648	3.2523	3.3526
- bottom \downarrow	13.6601	13.0901	11.8089	11.1159	10.8579	10.8154
SW flux	63.1709	60.3422	52.7777	49.0250	46.8944	47.3956
- top \uparrow	79.3886	75.9043	62.3987	61.6078	58.9609	59.6203
- bottom \uparrow	13.6354	12.9018	11.3199	10.4635	10.0865	10.0846
- bottom \downarrow	96.4886	92.2204	80.6146	75.0035	71.6357	72.4819
T_{2m}	2.2619	2.4536	2.6596	2.7026	2.8249	2.9405
Precipitation	1.5515	1.5170	1.3788	1.2800	1.1747	1.1479

696

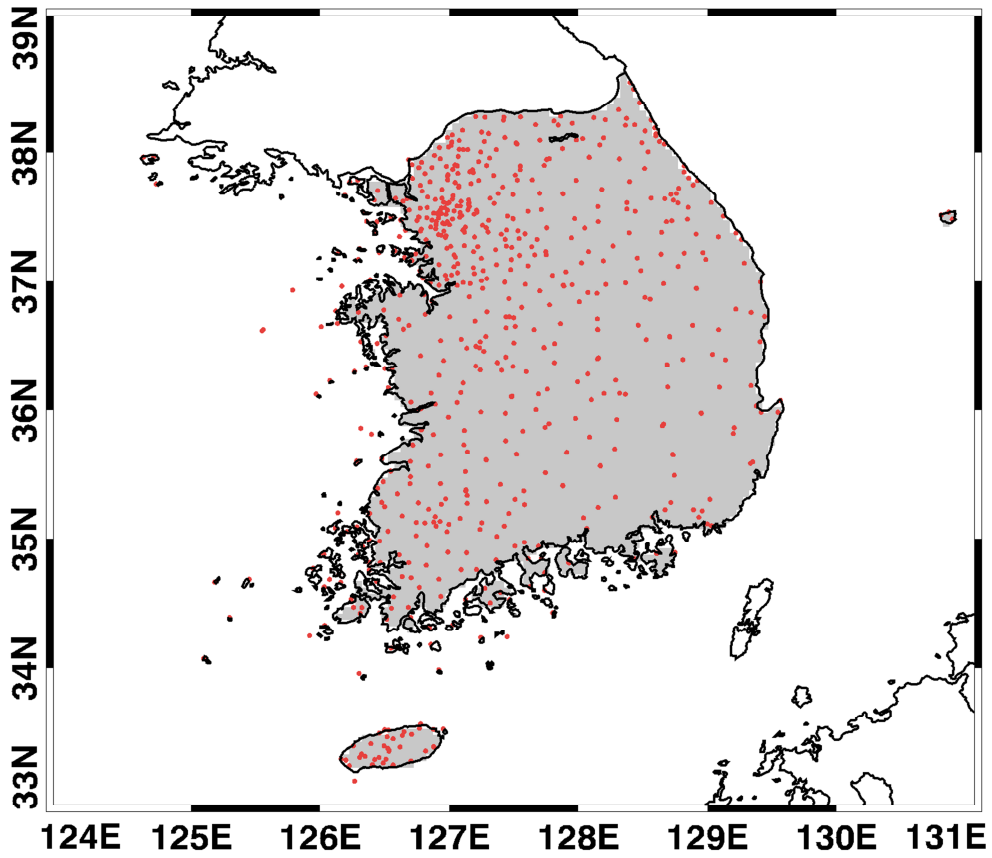
697

698 **Table 2.** Total root mean square error (RMSE) statistics for idealized squalline simulations.
699 The LW and SW heating rates [K day^{-1}], as well as the LW and SW fluxes [W m^{-2}], were
700 compared with the control simulations. The numbers before and after arrows indicate the
701 emulator only and the emulator with compound parameterization.

	LW heating rate	SW heating rate	LW flux	SW flux
5 km	3.59 → 2.61	1.65 → 1.21	21.33 → 16.57	193.19 → 160.76
3 km	4.42 → 2.96	2.48 → 1.64	34.02 → 16.06	260.52 → 154.19
2 km	4.29 → 2.98	2.32 → 1.33	23.69 → 17.65	225.13 → 147.67
1 km	5.19 → 3.87	3.37 → 1.75	37.39 → 16.09	291.27 → 104.46
0.5 km	5.90 → 4.49	3.30 → 1.75	47.59 → 15.60	269.50 → 101.52
0.25 km	5.29 → 3.44	2.99 → 1.43	43.36 → 16.01	245.47 → 174.04

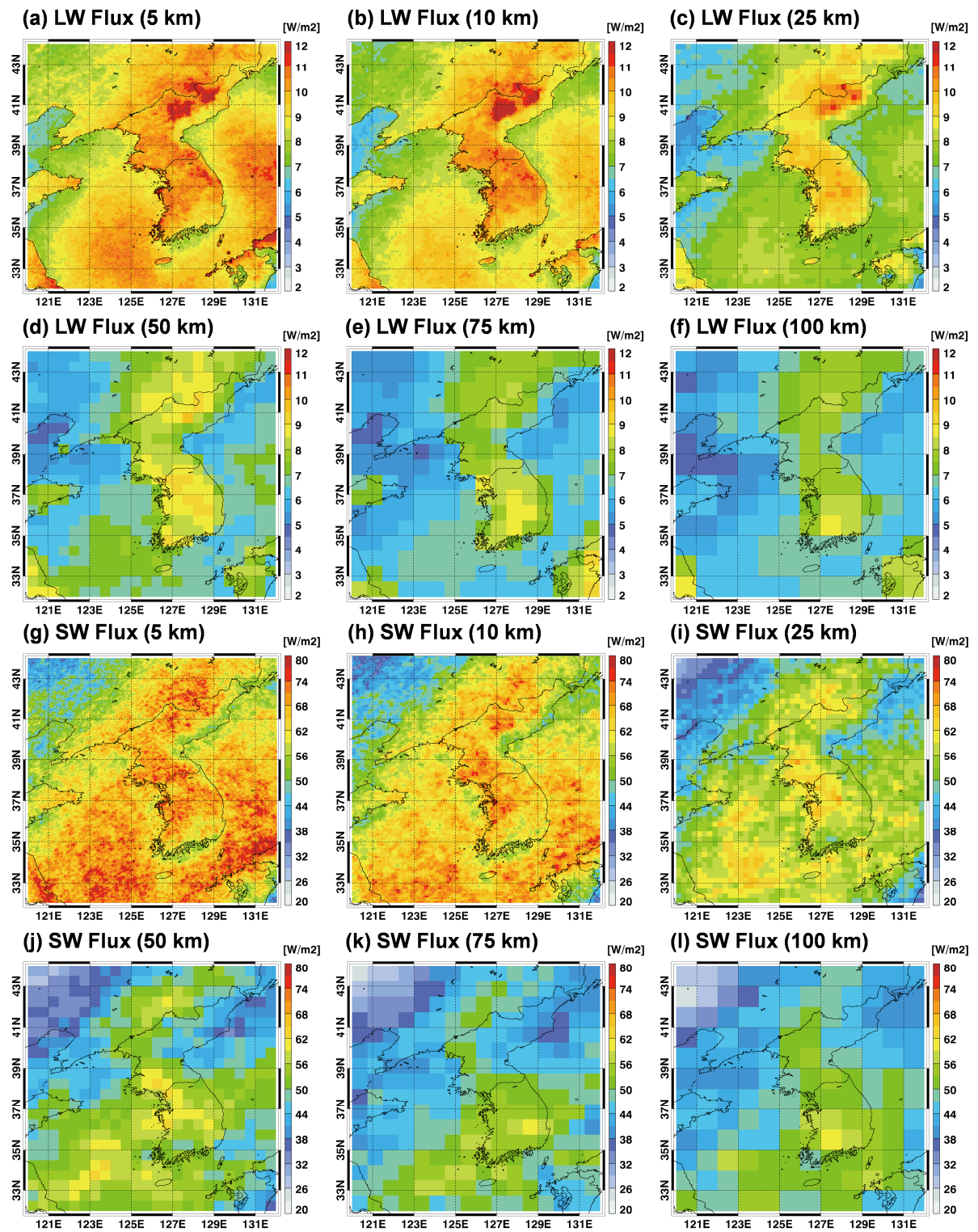
702

703



704
705 **Figure 1.** Locations of surface 713 stations (red circles) used for 2-m temperature along with
706 gauge-radar merged precipitation data with 5-km resolution (grey colors).

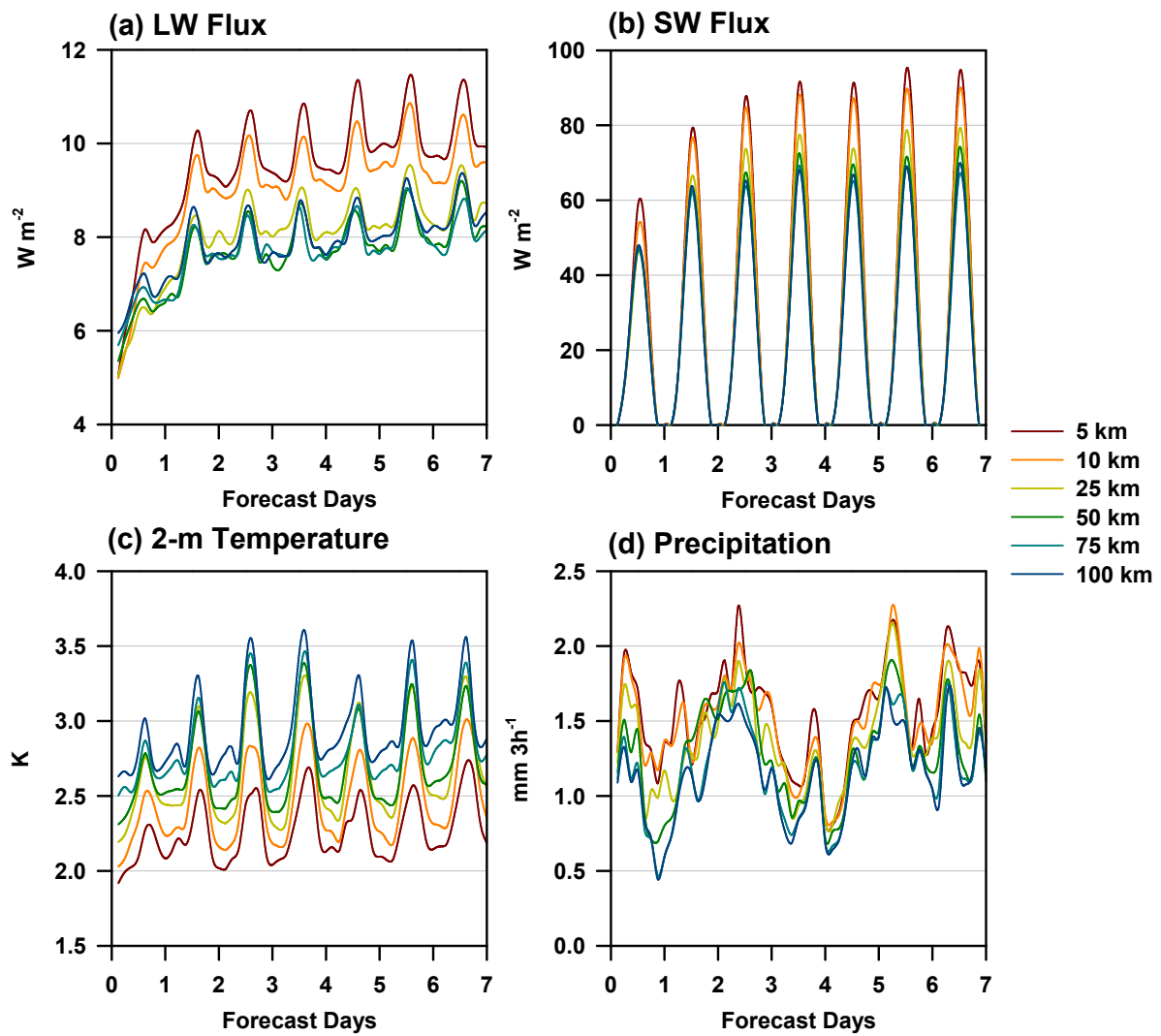
707



708
709
710

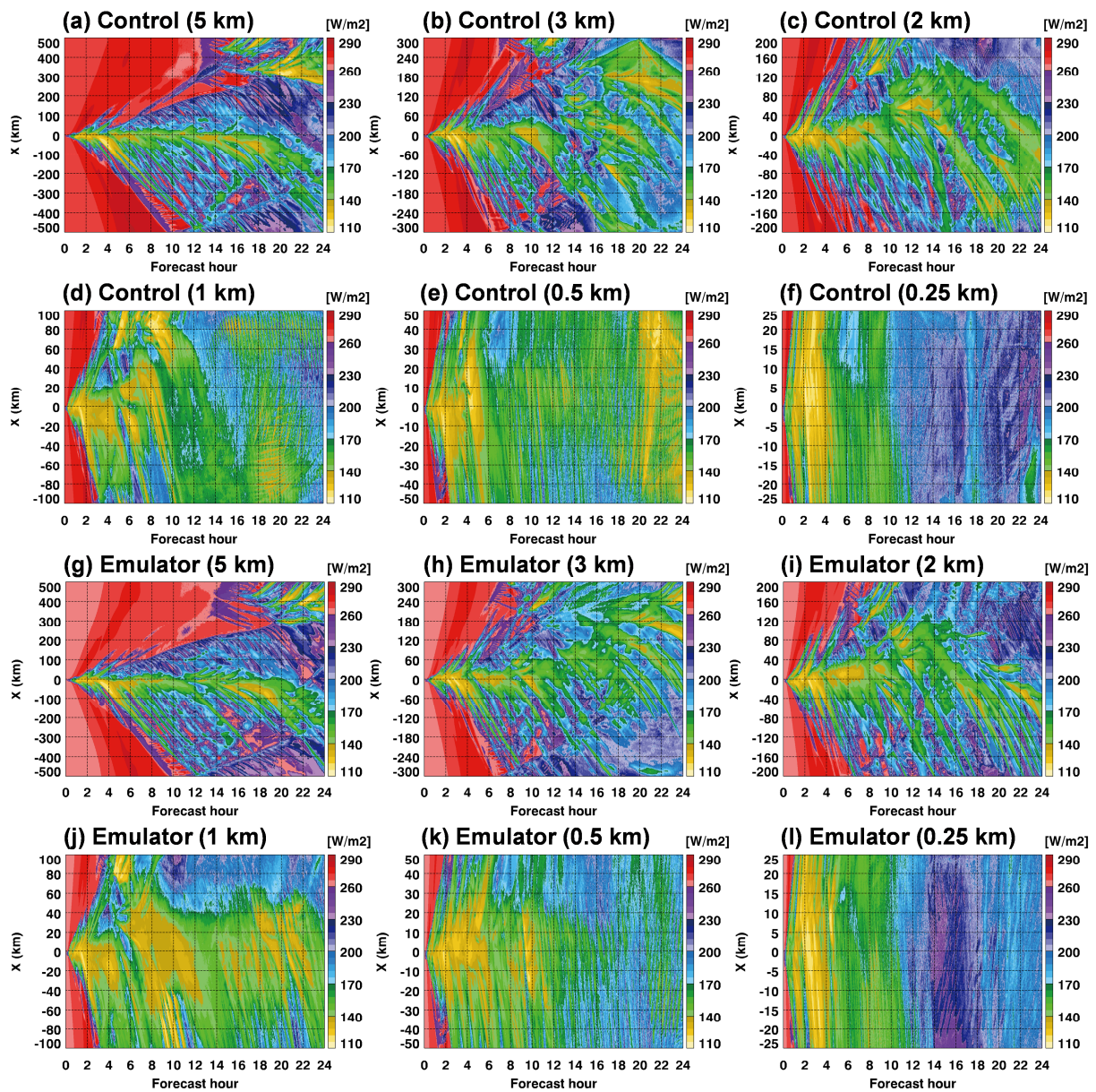
Figure 2. Spatial distributions of RMSEs for LW and SW fluxes compared to the control runs with different horizontal resolutions in real-case simulations.

711



712
 713 **Figure 3.** Time series of RMSEs for (a) LW and (b) SW fluxes compared to the control runs
 714 with different horizontal resolutions in real-case simulations. The results of (c) 2-m
 715 temperature and (d) 3 hourly precipitation compared with surface observations were also
 716 given.

717



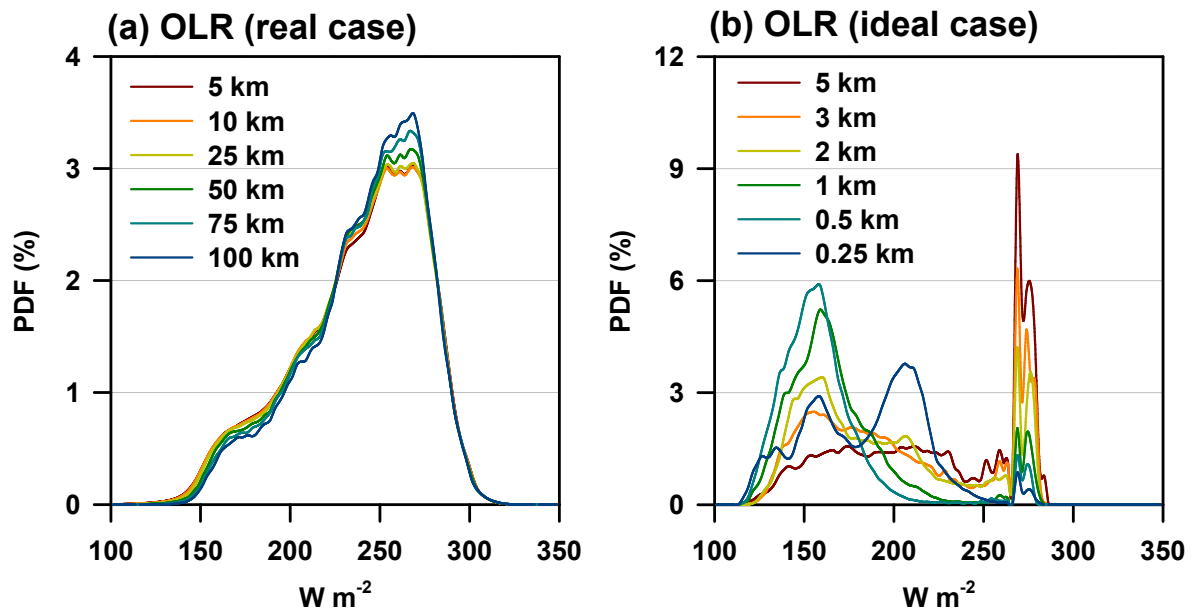
718

719

720

Figure 4. Spatio-temporal evolutions of outgoing longwave radiation (OLR) with different horizontal resolutions between control and emulator results in ideal-case simulations.

721



722

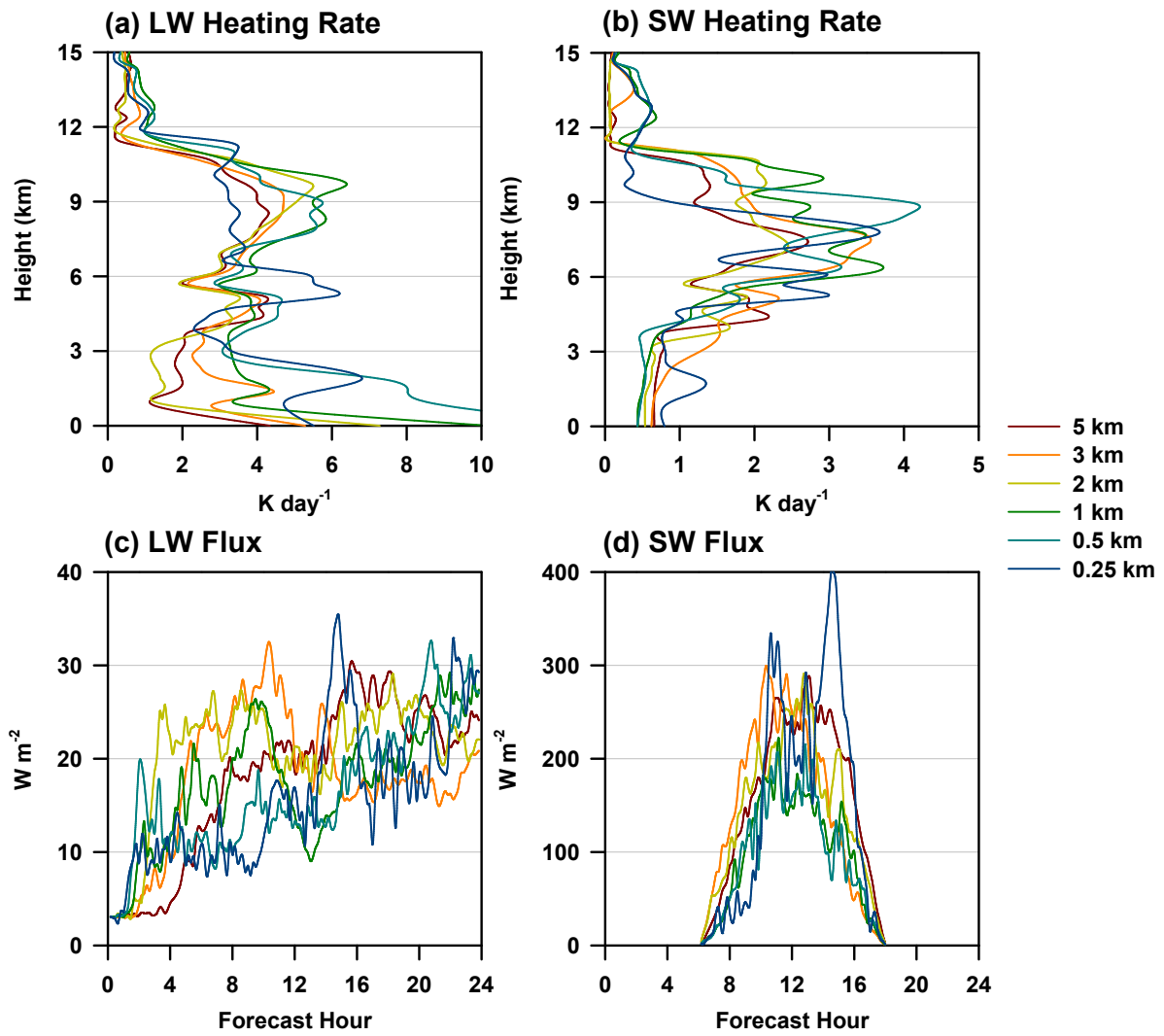
723

724 **Figure 5.** Probability density functions of outgoing longwave radiation (OLR) between (a)

724

real-case and (b) ideal-case simulations at different horizontal resolutions.

725



726
727
728
729

Figure 6. Vertical RMSEs of (a) LW and (b) SW heating rates, as well as temporal RMSEs of (c) LW and (d) SW fluxes, compared to the control runs with different horizontal resolutions in ideal-case simulations.